A three-mode self-referenced optical thermometry based on up/down-conversion luminescence of La3Mg2NbO9:Er3+,Yb3+ phosphors

Wu, Wenliang; Wang, Lei; Huang, Chenglan; Qu, Bingyan; Zhu, Caiping; Ding, Junxiang; Hintzen, Hubertus T.

DOI
10.1016/j.mtchem.2025.103317

Publication date
2026

Document Version
Final published version

Published in
Materials Today Chemistry

Materials Today Chemistry 51 (2026) 103317

Contents lists available at ScienceDirect

Materials Today Chemistry

journal homepage: www.journals.elsevier.com/materials-today-chemistry/

A three-mode self-referenced optical thermometry based on up/down-conversion luminescence of $La_3Mg_2NbO_9:Er^{3+},Yb^{3+}$ phosphors

Wenliang Wu [a], Lei Wang [a,d,*], Chenglan Huang [a], Bingyan Qu [a], Caiping Zhu [c], Junxiang Ding [a], Hubertus T. Hintzen [b,**]

[a] School of Materials Science and Engineering, Hefei University of Technology, Hefei, 230009, Anhui, China
[b] Fundamental Aspects of Materials and Energy, Delft University of Technology, Mekelweg 15, Delft, 2629 JB, Netherlands
[c] Henan Zhongyuan Expressway Co.,LTD, Zhengzhou, Henan, 450045, China
[d] Engineering Research Center of High Performance Copper Alloy Materials and Processing, Ministry of Education, Hefei University of Technology, Hefei, 230009, China

ARTICLE INFO

Keywords:
Photoluminescence
Three-mode luminescence thermometry
$La_3Mg_2NbO_9$
Self-referenced

ABSTRACT

Luminescence thermometry has garnered significant attention due to its rapid response and non-invasive nature. For practical multimodal thermometry that requires high sensitivity and anti-interference capability, single-system materials with high emission intensity are highly desirable. Herein, we report a three-mode optical thermometric material based on $La_3Mg_2NbO_9:Er^{3+}$, a double perovskite phosphor that exhibits intense green emissions centered at 527 and 547 nm under either 378 nm or 980 nm excitation. Co-doping with Yb^{3+} significantly enhances the up-conversion (UC) luminescence intensity of Er^{3+} by a factor of 3 and increases its down-conversion (DC) luminescence intensity by 5-fold. Furthermore, this phosphor demonstrates temperature-dependent sensitivity across UC luminescence, DC luminescence, and fluorescence lifetime modes. Thermometric performance evaluated via the fluorescence intensity ratio of the thermally coupled levels ($^2H_{11/2}$ and $^4S_{3/2}$) of Er^{3+} reveals outstanding behavior in both DC and UC modes over a broad temperature range (298–573 K), achieving maximum relative sensitivities of 1.16 % K^{-1} and 1.19 % K^{-1}, respectively. The fluorescence lifetime mode yields a maximum absolute sensitivity of 36.42 % μs K^{-1}. With excellent temperature sensitivity across all three modes, $La_3Mg_2NbO_9:Er^{3+}$ exhibits considerable potential for applications in self-referenced optical thermometry.

1. Introduction

Conventional contact-based thermometers, such as thermocouples and liquid-in-glass thermometers, are limited by slow response times and low sensitivity, which restricts their applicability in biomedical imaging, tissue analysis, and transportation monitoring [1–3]. In contrast, optical thermometry techniques offer significant advantages including rapid response, non-invasiveness, immunity to electromagnetic interference, and high sensitivity, making them highly suitable for remote and accurate temperature detection [4–7]. These methods primarily utilize temperature-dependent luminescence characteristics, including the fluorescence intensity ratio (FIR), fluorescence lifetime (FL), and emission band shifts [8]. Conventional single-mode thermometry typically relies exclusively on emissions from either up-conversion (UC) or down-conversion (DC) luminescence using FIR or FL techniques [9]. When excitation light is employed for temperature detection, a single emission signal becomes highly susceptible to environmental interference such as fluctuations in ambient absorption, variations in scattering effects and the differential absorption of ultraviolet (UV) or near-infrared (NIR) radiation by the sample itself [10]. These factors can lead to inaccurate readings, particularly in complex environments where a single signal may fail to provide reliable temperature information. To overcome these limitations, multi-mode thermometry, which integrates complementary sensing signals, has emerged as an effective strategy to enhance measurement accuracy and reliability [11]. This approach integrates multiple parameters, such as FIR under various excitations and FL, cross-referencing them to mitigate the negative impact of environmental fluctuations on measurement accuracy. By combining FIR readings obtained under UV and NIR excitation with FL measurements, this method significantly improves temperature

* Corresponding author. School of Materials Science and Engineering, Hefei University of Technology, Hefei, 230009, Anhui, China.
** Corresponding author.
E-mail addresses: leiwang@hfut.edu.cn (L. Wang), H.T.Hintzen@tudelft.nl (H.T. Hintzen).

https://doi.org/10.1016/j.mtchem.2025.103317
Received 5 November 2025; Received in revised form 19 December 2025; Accepted 21 December 2025
Available online 25 December 2025

Table 1
Sensing sensitivity based on the TCLs emission materials.

	Sensing materials		λ_{ex}	Temperature	Sa (K^{-1})	Sr (K^{-1})	Reference
TCLs	$K_3Y(PO_4)_2$:Yb^{3+}/Ho^{3+}	$^5F_5/^5F_4$	980 nm	303~523 K		0.0020	[41]
TCLs	$Gd_2Ti_2O_7$:Eu^{3+}	$^5D_1/^5D_0$	980 nm	303~423 K	0.015	0.0096	[43]
TCLs	$NaLuF_4$:Tm^{3+}	$^3F_{2,3}/^3H_4$	980 nm	250~600 K	0.00045	2386.93/T^2	[44]
TCLs	$K_3Y(PO_4)_2$:Yb^{3+}/Er^{3+}	$^4S_{3/2}/^2H_{11/2}$	980 nm	293~553 K	0.00304	0.0086	[41]
TCLs	$Na_{0.5}Bi_{0.5}TiO_3$:Yb^{3+}/Er^{3+}	$^4S_{3/2}/^2H_{11/2}$	980 nm	163~613 K	0.0031		[45]
TCLs	Bi_2SiO_5:Yb^{3+}/Er^{3+}	$^4S_{3/2}/^2H_{11/2}$	980 nm	298~600 K	0.00385	0.0099	[46]
TCLs	PbF_2:Er^{3+}/Yb^{3+}	$^4S_{3/2}/^2H_{11/2}$	980 nm	303~442 K	0.00434	0.0083	[47]
TCLs	$SrNb_2O_6$:Er^{3+}	$^4S_{3/2}/^2H_{11/2}$	980 nm	298~523 K	0.00615	1093.27/T^2	[48]
TCLs	Y_2O_3:Er^{3+}	$^4F_{9/2}/^2H_{11/2}$	980 nm	298~393 K	0.00013	630.67/T^2	[49]
TCLs	GdPVO$_4$: Er^{3+}/Yb^{3+}	$^4S_{3/2}/^2H_{11/2}$	325 nm	300~510K	0.006012	0.0085	[19]
TCLs	$SrLaLiWO_6$:Er^{3+}, Yb^{3+}	$^4S_{3/2}/^2H_{11/2}$	380 nm	303~573K	0.0095	0.0091	[12]
TCLs	$BaLaLiWO_6$:Er^{3+}, Yb^{3+}	$^4S_{3/2}/^2H_{11/2}$	380 nm	303~573K	0.0078	0.0073	[12]
TCLs	$La_3Mg_2NbO_9$:Er^{3+}	$^4S_{3/2}/^2H_{11/2}$	378 nm	298~573K	0.00679	0.0108	This work
TCLs	$La_3Mg_2NbO_9$:Er^{3+},Yb^{3+}	$^4S_{3/2}/^2H_{11/2}$	378 nm	298~573K	0.00754	0.0116	This work
TCLs	$La_3Mg_2NbO_9$:Er^{3+}	$^4S_{3/2}/^2H_{11/2}$	980 nm	298~573K	0.00647	0.0119	This work
TCLs	$La_3Mg_2NbO_9$:Er^{3+},Yb^{3+}	$^4S_{3/2}/^2H_{11/2}$	980 nm	298~573K	0.00785	0.0115	This work
FL	$Ba_2SrLu_4O_9$:Yb^{3+}/Er^{3+}	$^4S_{3/2}$	980 nm	323~573K	0.0452μs	0.00087	[50]
FL	$La_2Mo_3O_{12}$:Yb^{3+}/Er^{3+}	$^2H_{11/2}$	373 nm	303~573K	0.062μs	0. 0028	[51]
FL	$La_3Mg_2NbO_9$:Er^{3+}	$^4S_{3/2}$	378 nm	298~573K	0.3642μs	0.0038	This work
FL	$La_3Mg_2NbO_9$:Er^{3+}	$^2H_{11/2}$	378 nm	298~573K	0.2569μs	0.0028	This work

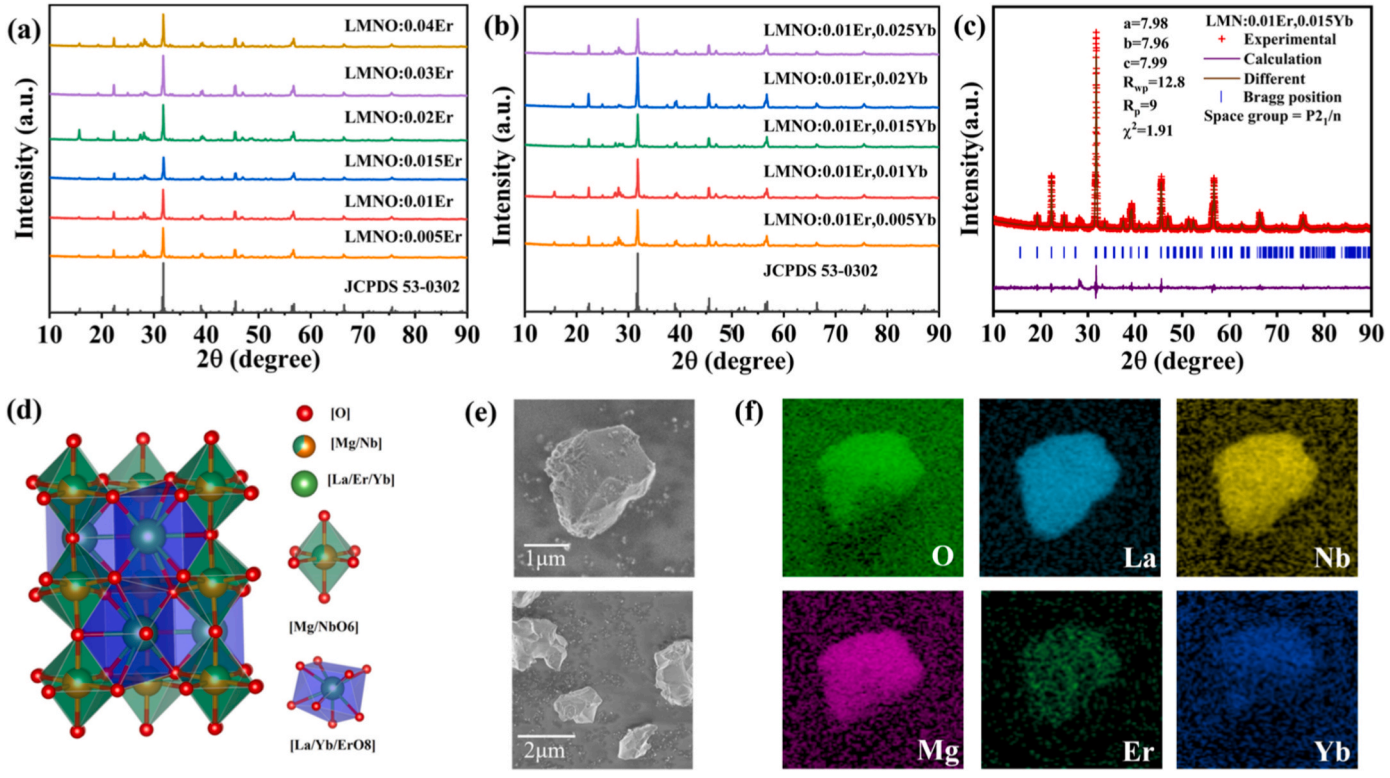

Fig. 1. XRD patterns of (a) LMNO:$x$$Er^{3+}$ ($0.005 \leq x \leq 0.04$) and (b) LMNO:0.01Er^{3+},$y$$Yb^{3+}$($0.005 \leq y \leq 0.025$); (c) The Rietveld refinement profile of LMNO:0.01Er^{3+}, 0.015 Yb^{3+}; (d) Schematic crystal structure of LMNO; (e) SEM images and (f) elemental mapping of LMNO:0.01Er^{3+}, 0.015 Yb^{3+}.

sensing in complex environments (See Table 1)[12]. More importantly, employing multiple luminescent thermometric modes within a single phosphor transcends mere interference reduction. It establishes an inherent cross-verification strategy, providing built-in redundancy against potential single-point signal failures, such as those induced by scattering or excitation source instability. This intrinsic multi-modal cross-checking mechanism directly substantiates the robustness and reliability of our self-referenced optical thermometer.

Among various luminescent centers, Er^{3+} has garnered significant research interest in the field of optical thermometry, as exemplified by materials such as La_2MoO_6:Er^{3+} [13], Ca_2MgWO_6:Er^{3+} [14], $NaGdF_4$:Er^{3+} [15] and YVO_4: Er^{3+} [3]. This is attributed to its distinct energy level structure, such as the $^2H_{11/2}$ and $^4S_{3/2}$ states, which enables both UC and DC luminescence within a single host material [16]. This property allows for robust multi-mode temperature sensing, primarily utilizing the FIR technique between thermally coupled levels (TCLs) [17]. Consequently, Er^{3+}-doped materials are considered highly promising for achieving high-precision temperature readings in complex and interfering environments [18,19]. However, the absorption efficiency of Er^{3+} at 980 nm is intrinsically limited due to the forbidden nature of 4f–4f transitions [20]. Low emission intensity severely compromises temperature measurement reliability, as the weak signal is susceptible to detector noise, causing significant uncertainties in the calculated FIR. To address this, Yb^{3+} is frequently co-doped as a sensitizer to enhance its

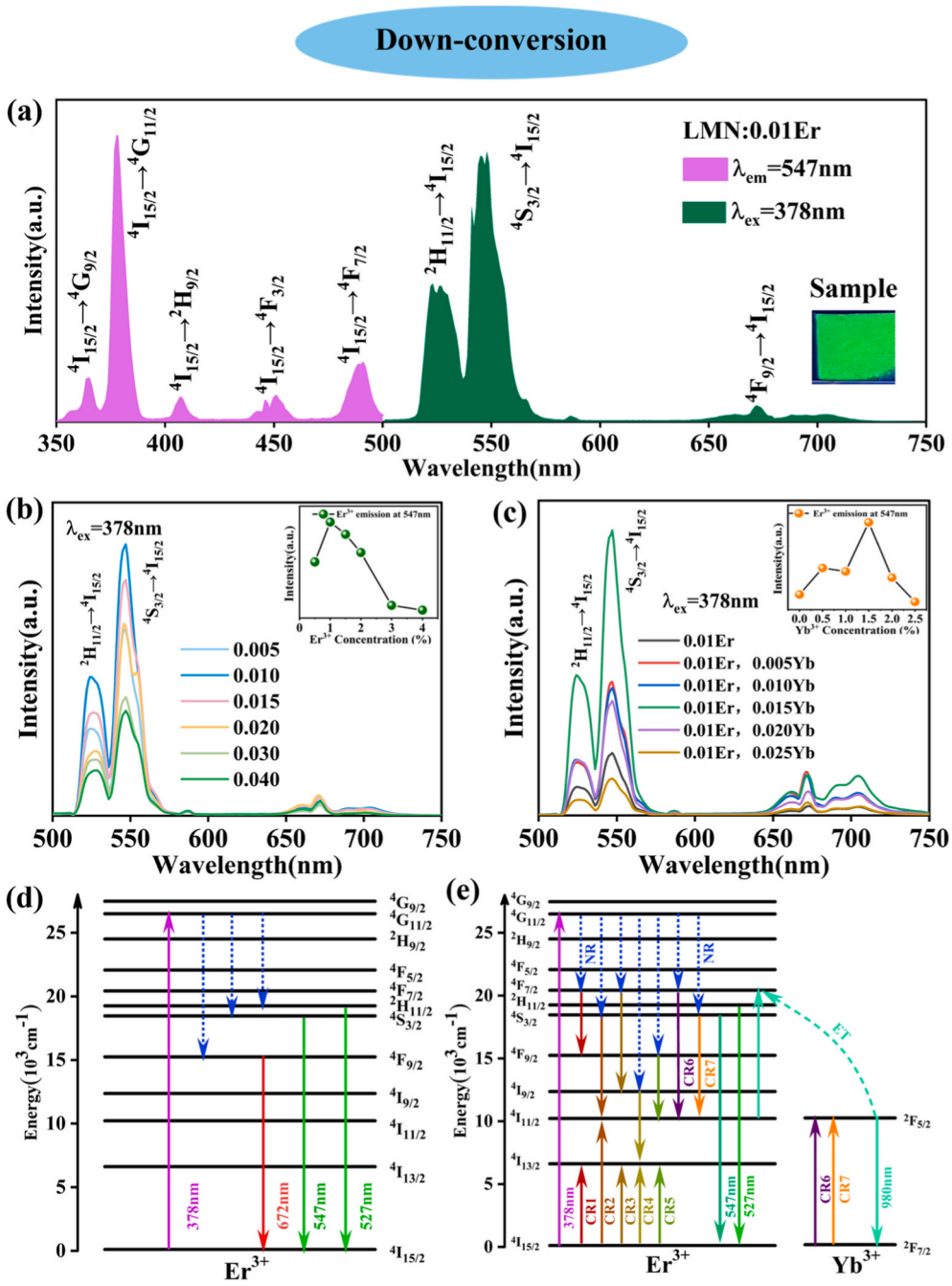

Fig. 2. (a) The PLE and PL emission spectra of LMNO:0.01Er^{3+} (inset: photographs of LMNO:0.01Er^{3+} sample under 365 nm light); The PL emission spectra of (b) LMNO:xEr^{3+} ($0.005 \leq x \leq 0.04$) and (c) LMNO:0.01Er^{3+}, yYb^{3+} ($0.005 \leq y \leq 0.025$); (d, e) Energy level diagram of Er^{3+} and Yb^{3+} in LMNO under 378 nm excitation, CRi (i = 1–7) denotes the possible transitions.

near-infrared absorption rate and subsequent emission intensity in Er^{3+}-doped phosphors, such as $YNbO_4$:Er^{3+},Yb^{3+} [21]. This makes Er^{3+}/Yb^{3+} co-doped systems highly promising for UC thermometry [22,23].

Of the various host materials for Er^{3+}-activated luminescence, niobates have attracted notable interest due to their exceptional chemical stability, low phonon energy, and high emission intensity [24,25]. Furthermore, niobate-based hosts show potential for multimodal thermometry due to their unique capability of being efficiently excited by both UV and near-infrared NIR radiation. For instance, Ca_2GaNbO_6:Er^{3+} enables luminescence lifetime thermometry under 379 nm excitation [26], while $YNbO_4$:Er^{3+}/Yb^{3+} permits UC sensing up to 820 K under 980 nm laser irradiation [27]. This dual excitability positions niobates as ideal candidates for developing advanced multimodal luminescent thermometers. Among the niobate family, $La_3Mg_2NbO_9$, the crystal structure was first elucidated by J. S. Kim et al., in 1999 [28]. The niobate-based host $La_3Mg_2NbO_9$ possesses a stable double perovskite structure, which provides a rigid crystal framework and a modifiable local crystal field. It can effectively suppress phonon-assisted energy loss and significantly enhance luminescence efficiency, making it a particularly suitable host for luminescent ions [29,30]. When doped with ions such as Sm^{3+} [31], the luminescent properties enabled by these structural advantages have been demonstrated. More importantly for optical thermometry, recent work by Yang, Z.F. et al. [32] has successfully utilized this host by co-doping with Sm^{3+}/Mn^{4+} to create a dual-mode thermometer, directly proving the inherent suitability of $La_3Mg_2NbO_9$

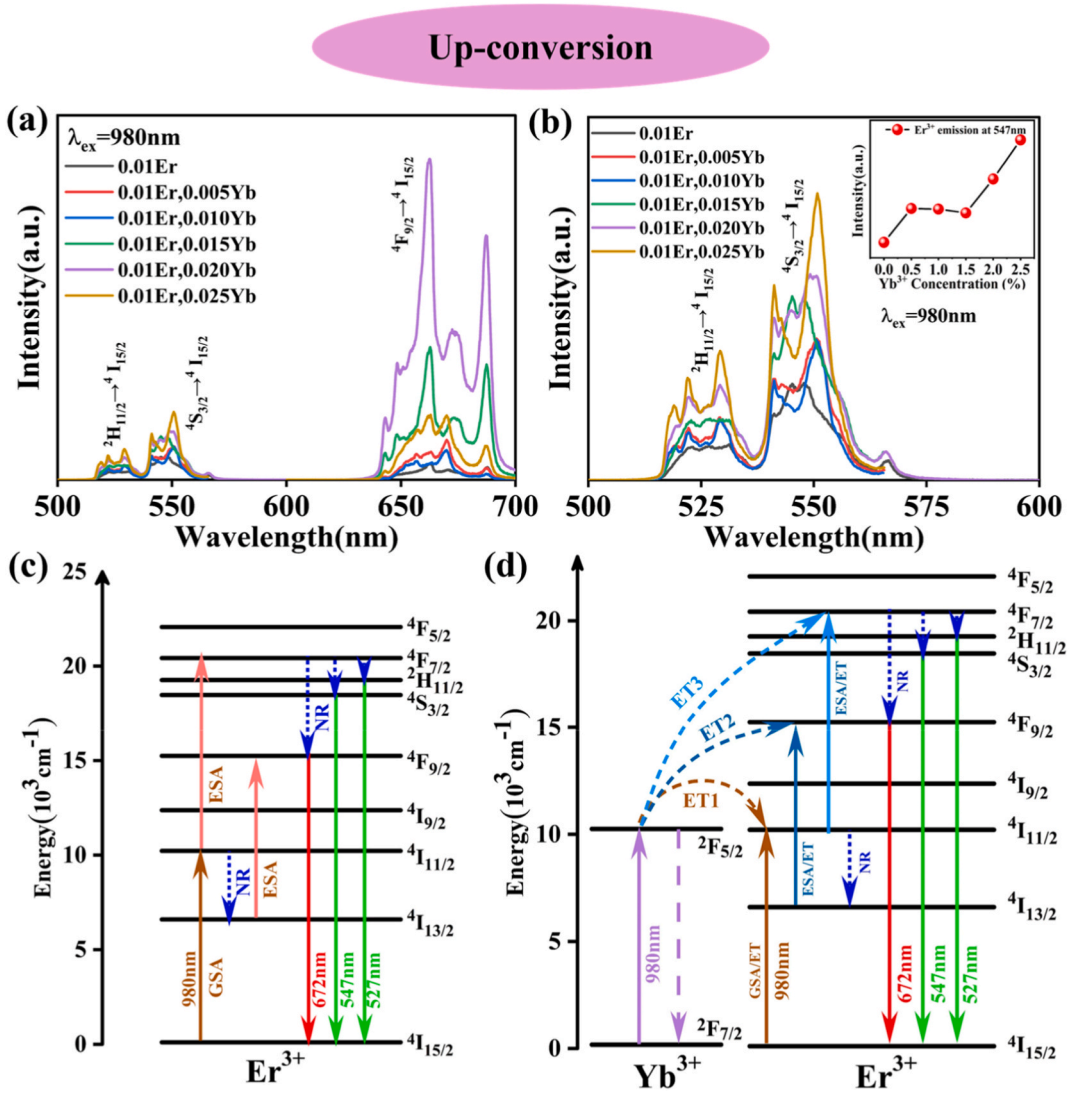

Fig. 3. (a, b) PL spectra of LMNO:0.01Er^{3+}, yYb^{3+} ($0.005 \leq y \leq 0.025$); (c, d) Energy level diagram of Er^{3+} and Yb^{3+} in LMNO under 980 nm excitation.

and its potential for developing self-referenced sensing platforms. However, both the luminescence behavior of Er^{3+} in this host matrix and its potential for optical temperature sensing have not been reported.

In this work, we developed a optical thermometer based on the luminescence of Er^{3+}/Yb^{3+} co-doped $La_3Mg_2NbO_9$ (LMNO), which exhibit both intense DC and UC luminescence. Under excitations at either 378 nm or 980 nm, the phosphor emits characteristic green light comprising two distinct bands centered at 527 nm and 547 nm, corresponding to the $^2H_{11/2} \rightarrow {}^4I_{15/2}$ and $^4S_{3/2} \rightarrow {}^4I_{15/2}$ transitions of Er^{3+}, respectively. The incorporation of Yb^{3+} not only acts as an effective sensitizer for UC processes, boosting the UC emission intensity by 3 times, but also remarkably enhances the DC emission intensity by a factor of 5. More importantly, both the DC and UC emission signals exhibit strong temperature dependence, making them viable for thermometric applications. The maximum relative sensitivity achieved based on the FIR of the DC and UC emissions reaches 1.16 % K^{-1} and 1.19 % K^{-1} respectively. Additionally, the temperature-dependent FL of Er^{3+} under 378 nm excitation also demonstrates excellent performance, yielding a maximum absolute sensitivity of 36.42 % μs^{-1} K^{-1}. Collectively, these indicate that LMNO: Er^{3+}, Yb^{3+} phosphor is a promising candidate for triple-mode thermometry (UC-FIR, DC-FIR, and DC-FL), enabling reliable self-referenced temperature detection in complex environments.

2. Experimental section

2.1. Materials and synthesis

LMNO:xEr^{3+} and LMNO:0.01Er^{3+}, yYb^{3+} (x = 0.005, 0.01, 0.015, 0.02, 0.03, 0.04, y = 0.005, 0.01, 0.015, 0.02, 0.025) phosphors were prepared via a high-temperature solid-state reaction method. Starting materials, MgO (99.99 %), La_2O_3 (99.9 %), Nb_2O_5 (99.9 %), Er_2O_3 (99.9 %) and Yb_2O_3 (99.9 %) were stoichiometrically weighed and uniformly mixed in an agate mortar and then sintered in a muffle furnace at 700 °C for 5 h. Subsequently, the precursors were calcined at 1400 °C for 7 h and cooled down to ambient temperature for grinding and performing characterizations.

2.2. Characterization

The phases of the samples are confirmed through X-ray diffraction (XRD) measurement with a Smartlab series diffractometer (Rigaku Corporation, Japan) using Cu Kα radiation in the 2θ range from 10° to 90°. Structural refinements were conducted using the General Structure Analysis System (GSAS2) software. The morphology and elements of the samples were characterized by thermal field-emission scanning electron microscope (SEM) (Gemini 500, Carl Zeiss AG, Germany). The emission spectra (PL), excitation spectra (PLE), FL spectra and temperature-

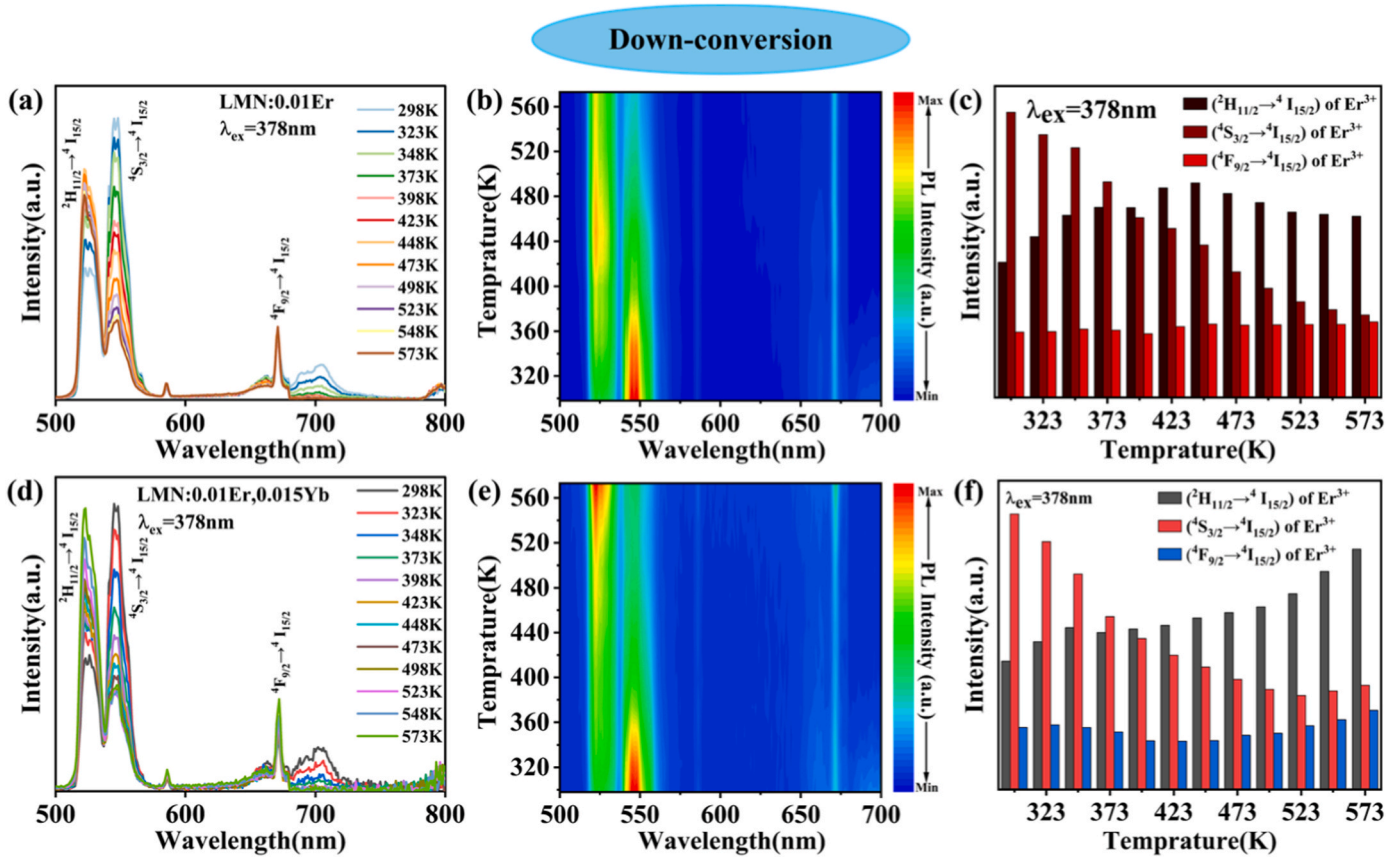

Fig. 4. Temperature-dependent PL spectra, the corresponding contour maps and normalized integration PL intensity of (a–c) LMNO:0.01Er^{3+} and (d–f) LMNO:0.01Er^{3+},0.015 Yb^{3+}. Integration ranges: 515–537 nm ($^2H_{11/2} \rightarrow {}^4I_{15/2}$); 537–575 nm ($^2H_{11/2} \rightarrow {}^4I_{15/2}$).

dependent emission spectra were measured with a fluorescence spectrophotometer (FS5, Edinburgh Instruments, UK) equipped with a 150 W xenon lamp, 380-nm and 980-nm lasers (each with an output power of 2 W) and a temperature-control platform in the range of 273–573 K.

3. Results and discussion

3.1. Structure and composition characterizations

Phase purity and crystal structure of the synthesized LMNO:$x$$Er^{3+}$ ($0.005 \leq x \leq 0.04$) and LMNO:0.01Er^{3+},$y$$Yb^{3+}$ ($0.005 \leq y \leq 0.025$) phosphors are confirmed by XRD analysis (Fig. 1a and b). All diffraction patterns exhibit monophasic characteristics matching the standard $La_3Mg_2NbO_9$ phase (PDF#53–0302) without detectable impurities. The crystal structure of LMNO (Fig. 1d) features La^{3+} ions in [LaO_8] polyhedra, while Mg^{2+} and Nb^{5+} occupy edge-sharing [MgO_6] and [NbO_6] octahedra. Rietveld refinement for the sample of LMNO:0.01Er^{3+},0.015 Yb^{3+} as shown in Fig. 1c yielded its refined convergence ($R_p = 9$ %, $R_{wp} = 12.8$ %, $\chi^2 = 1.91$), confirming phase purity and structural integrity. Given their comparable ionic radii (r(Er^{3+}) = 1.004 Å, r(Yb^{3+}) = 0.985 Å compared to r(La^{3+}) = 1.16 Å at CN = 8) [33], both rare-earth ions preferentially substitute at La^{3+} sites.

Concurrently, the morphological characteristics of the phosphor samples are investigated. Fig. 1e displays a representative SEM image of the LMNO:0.01Er^{3+},0.015 Yb^{3+} sample. The particles exhibit irregular shapes with an average size of about 2–5 μm, characteristic of samples prepared via the high-temperature solid-state reaction method. EDS mapping analysis (Fig. 1f) confirms the homogeneous distribution of La, Nb, Mg, O, Er and Yb throughout the particles, with no obvious elemental segregation.

3.2. DC and UC luminescence properties

Fig. 2a shows the PL spectrum of LMNO:0.01Er^{3+} phosphor under 378 nm excitation, presenting the characteristic emission peaks of Er^{3+}, with the peaks located at 527, 547 and 672 nm, which are attributed to the characteristic emissions of $^2H_{11/2} \rightarrow {}^4I_{15/2}$, $^4S_{3/2} \rightarrow {}^4I_{15/2}$ and $^4F_{9/2} \rightarrow {}^4I_{15/2}$ respectively [34]. In addition, Fig. 2a also shows the PLE spectra of LMNO:Er^{3+} phosphor. Monitored at 547 nm, five characteristic excitation peaks are observed at 365, 378, 407, 451 and 491 nm, which are respectively attributed to the characteristic transitions of $^4I_{15/2} \rightarrow {}^4G_{9/2}$, $^4I_{15/2} \rightarrow {}^4G_{11/2}$, $^4I_{15/2} \rightarrow {}^2H_{9/2}$, $^4I_{15/2} \rightarrow {}^4F_{3/2}$ and $^4I_{15/2} \rightarrow {}^4F_{7/2}$ of Er^{3+} ions. As illustrated in the energy-level diagram (Fig. 2d), upon 378 nm excitation, the Er^{3+} ions are excited from the ground state ($^4I_{15/2}$) to the excited state ($^4G_{11/2}$), followed by non-radiative relaxation to the $^2H_{11/2}$, $^4S_{3/2}$ and $^4F_{9/2}$ levels. Subsequent radiative transitions to the ground state ($^4I_{15/2}$) yield two strong green bands locating at 527 and 547 nm and a weak red band with maximum at 672 nm.

The DC spectra of LMNO:$x$$Er^{3+}$ ($0 \leq x \leq 0.040$) and LMNO:0.01Er^{3+}, $y$$Yb^{3+}$ ($0.005 \leq y \leq 0.025$) sample are shown in Fig. 2b and c. In Er^{3+} singly-doped sample, the intensity of both green bands increases with Er^{3+} concentration, until $x = 0.01$, then decreases due to concentration quenching. Notably, Yb^{3+} co-doping significantly enhances their green emission intensity (Fig. 2c), with optimal intensity observed at $y = 0.015$, approximately five-fold higher than LMNO:0.01Er^{3+} phosphor. This enhancement arises from cross-relaxation (CR) and cooperative energy transfer (CET) between Er^{3+} and Yb^{3+} [35]. The energy level diagram in Fig. 2e shows the possible cross relaxation processes during the emission of Yb^{3+} and Er^{3+}. In Er^{3+} singly-doped sample, multiple Er^{3+}-Er^{3+} cross-relaxation (CR1-CR5) dominate, which reduce the quantum yields of $^2H_{11/2} \rightarrow {}^4I_{15/2}$ and $^4S_{3/2} \rightarrow {}^4I_{15/2}$ transitions. When co-doped with Yb^{3+}, two extra cross-relaxation modes (CR6 and CR7, as

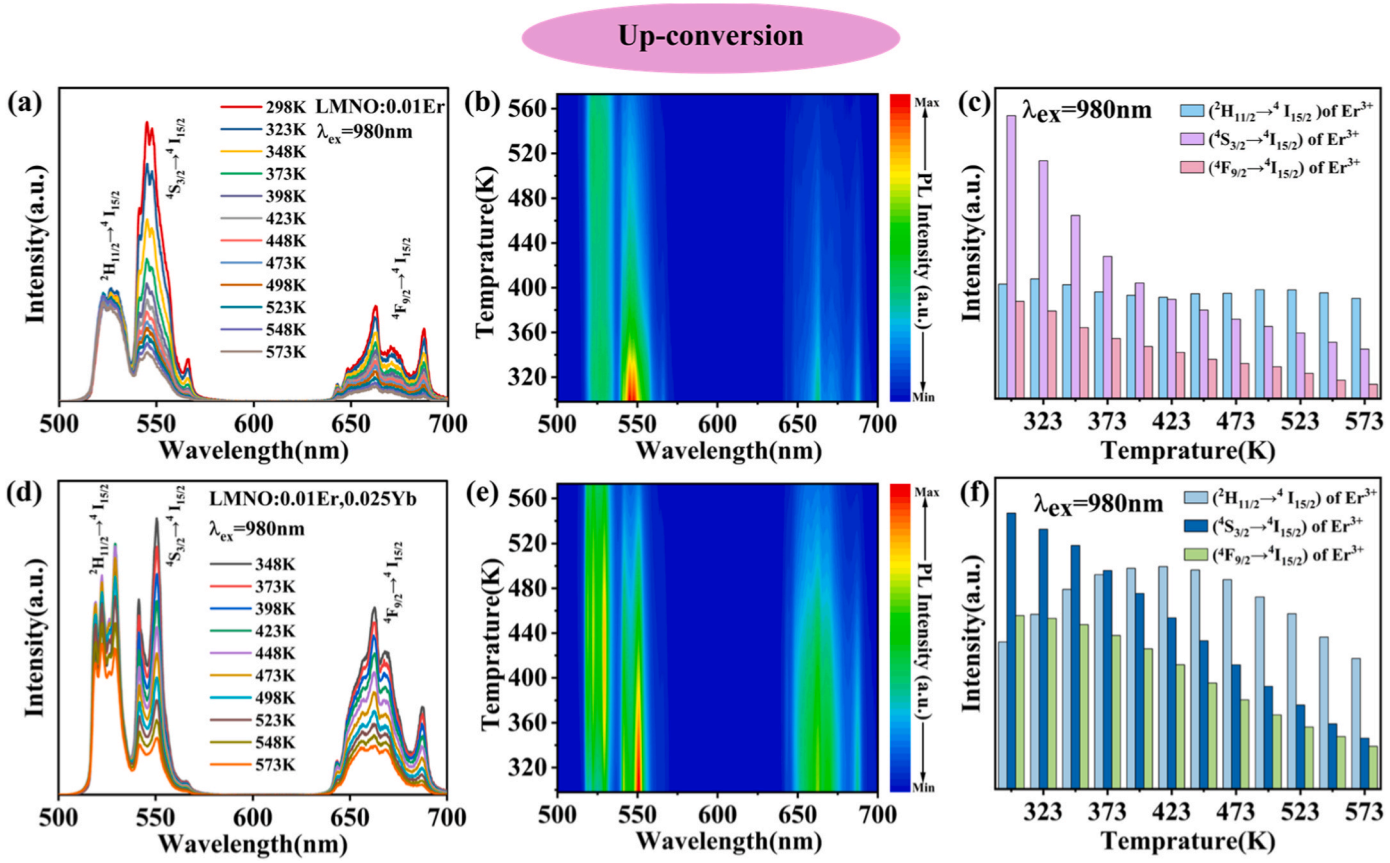

Fig. 5. Temperature-dependent PL spectra, the corresponding contour maps and normalized integration PL intensity of (a–c) LMNO:0.01Er^{3+} and (d–f) LMNO:0.01Er^{3+},0.025 Yb^{3+}. Integration ranges: 515–537 nm ($^2H_{11/2} \rightarrow {}^4I_{15/2}$); 537–575 nm ($^2H_{11/2} \rightarrow {}^4I_{15/2}$).

depicted in Fig. 2e) will emerge. Subsequently, energy transfer takes place between Yb^{3+} and Er^{3+}: $^2F_{5/2}$ (Yb^{3+}) + $^4I_{11/2}$ (Er^{3+}) → $^4F_{7/2}$ (Er^{3+}) + $^2F_{7/2}$ (Yb^{3+}), which boosts green emission. In simple terms, Yb^{3+} suppress Er^{3+}-Er^{3+} cross-relaxation, thereby increasing the population of $^4F_{7/2}$ levels in Er^{3+}. However, when Yb^{3+} concentration is higher than 0.015, self-quenching will occur. Simultaneously, the energy transfer between Yb^{3+} ions will be intensified, resulting in the weakening of the energy transfer between Er^{3+} and Yb^{3+} ions and the intensity of green emission decrease [36].

Subsequently, the UC luminescence properties of LMNO:Er^{3+}, Yb^{3+} phosphors were investigated. Their emission spectra and the maximum intensities dependence on Yb^{3+} concentrations under 980 nm excitation are shown in Fig. 3a. It can be clearly observed that the presence of Yb^{3+} ions can enhance the UC luminescence of Er^{3+} ions, especially the red-light emission intensity of Er^{3+} at 672 nm ($^4F_{9/2} \rightarrow {}^4I_{15/2}$). To better observe the variation of Er^{3+}'s green emission intensity with concentration, Fig. 3b is an enlarged view of Fig. 3a in the range of 500–600 nm. The emission intensities of Er^{3+} at 527 nm ($^2H_{11/2} \rightarrow {}^4I_{15/2}$) and 547 nm ($^4S_{3/2} \rightarrow {}^4I_{15/2}$) increase with the increase of Yb^{3+} ions concentration. This indicates that the presence of Yb^{3+} can increase both the DC and UC green emissions of Er^{3+}.

To better understand this observation, the energy-level diagrams of Er^{3+} and Yb^{3+} regarding UC emission are presented. As depicted in Fig. 3c, upon 980 excitation, the transition of $^4I_{15/2} \rightarrow {}^4I_{11/2}$ takes place via ground-state absorption (GSA) of Er^{3+} and then part of the energy relaxes non-radiatively to the $^4I_{13/2}$ energy level [27]. Meanwhile, excited states of $^4I_{11/2}$ and $4I_{13/2}$ could transit to $^4F_{7/2}$ and $^4F_{9/2}$ energy levels through excited state absorption (ESA), respectively. Subsequently, the $^4F_{7/2}$ energy level relaxes non-radiatively to the $^2H_{11/2}$, $^4S_{3/2}$, $^4F_{9/2}$ energy levels and then radiatively transitions back to the ground state energy level ($^4I_{15/2}$). As shown in Fig. 3d [37], when Yb^{3+} and Er^{3+} are co-doped, the Yb^{3+} ions in ground state ($^2F_{7/2}$) are pumped to excited state ($^2F_{5/2}$) by 980 nm laser, then they transfer energy to the $^4I_{11/2}$, $^4F_{9/2}$ and $^4F_{7/2}$ energy levels of Er^{3+} ions respectively through energy transfer (ET1, ET2, ET3), thereby enhancing the green-light and red-light emissions of Er^{3+} ions.

In conclusion, the optimal concentration of Yb^{3+} for maximizing the emission intensity of DC (0.015) and UC (0.025) is different. The difference in the optimal doping concentration stems from their fundamentally different excitation mechanisms. Under 378 nm excitation, the DC process predominantly involves direct excitation of Er^{3+} ions, with Yb^{3+} acting mainly as an auxiliary co-dopant for potential cross-relaxation. Consequently, a lower Yb^{3+} concentration suffices to achieve emission saturation, beyond which concentration quenching rapidly prevails due to enhanced non-radiative energy migration among Yb^{3+} ions. In contrast, the UC emission under 980 nm excitation relies critically on Yb^{3+} as the primary sensitizer to absorb incident photons and subsequently transfer energy to Er^{3+}. A higher Yb^{3+} concentration (0.025) is necessary to maximize the absorption cross-section and the efficiency of the multi-step energy transfer processes required for populating the Er^{3+} emitting state.

3.3. *Temperature sensing based on DC and UC fluorescence thermometer*

Fig. 4a and d depict the DC temperature-dependent emission spectra of LMNO:0.01Er^{3+} and LMNO:0.01Er^{3+},0.015 Yb^{3+} phosphors under 378 nm excitation, with corresponding thermal evolution profiles shown in Fig. 4c and f. The temperature-dependent emission intensities at 527 nm ($^2H_{11/2} \rightarrow {}^4I_{15/2}$), 547 nm ($^4S_{3/2} \rightarrow {}^4I_{15/2}$) and 671 nm ($^4F_{9/2} \rightarrow {}^4I_{15/2}$) are illustrated in Fig. 4b and e. Notably, for Er^{3+}-only doping, the emission intensities at 547 nm decrease with rising temperature, while the 527 nm emission intensity increases progressively, reaching a

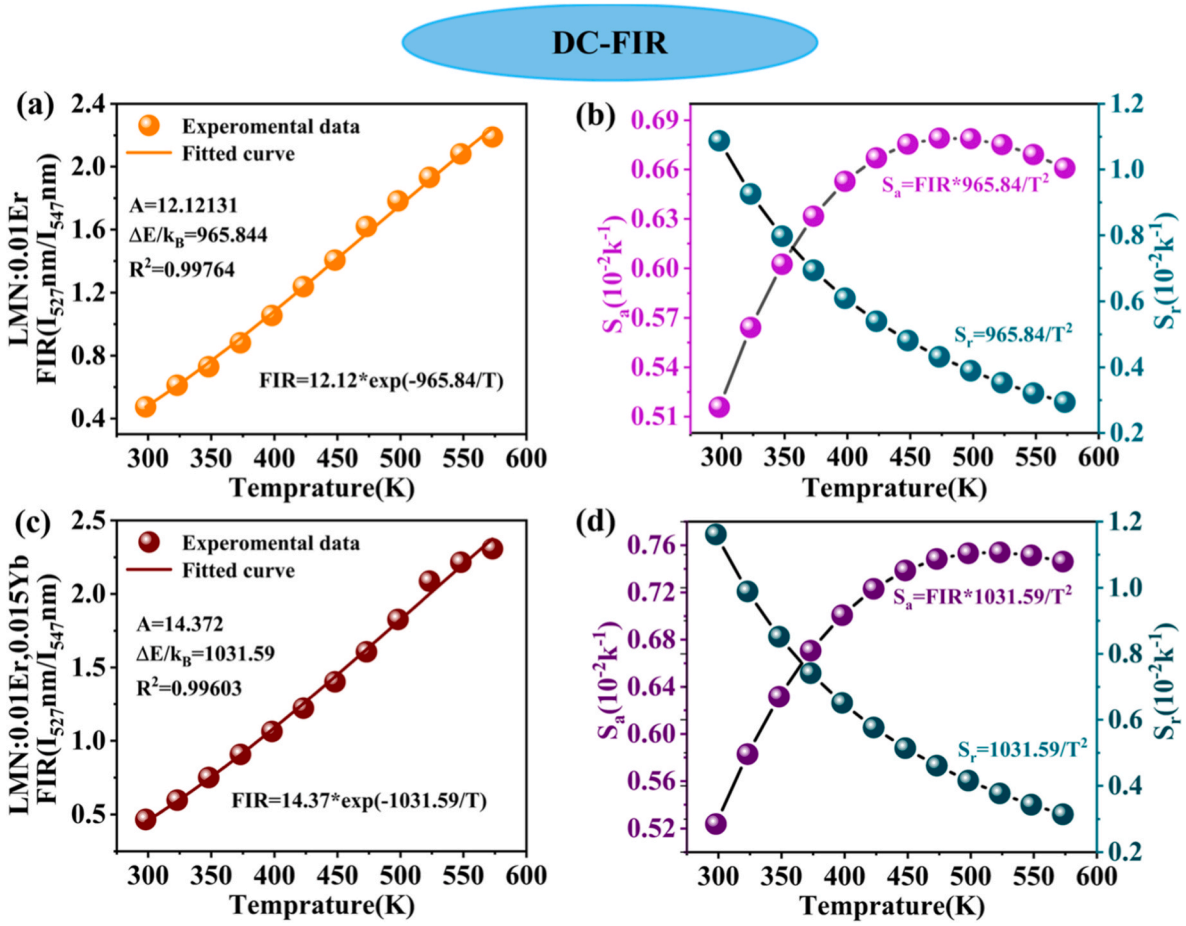

Fig. 6. FIR, S_a and S_r values calculated at different temperatures of (a, b) LMNO:0.01Er^{3+} and (c, d) LMNO:0.01Er^{3+},0.015 Yb^{3+} phosphor under 378 nm excitation.

maximum at 448 K. This behavior arises from the thermal population redistribution between the closely spaced $^2H_{11/2}$ and $^4S_{3/2}$ energy levels (theoretical energy gap: 694 cm^{-1}). At temperature elevated, population accumulated in $^4S_{3/2}$ is thermally excited to $^2H_{11/2}$, thereby enhancing the spontaneous emission probability of the corresponding 527 nm ($^2H_{11/2} \rightarrow {}^4I_{15/2}$) transition. For Er^{3+} and Yb^{3+} co-doped samples (Fig. 4e), the $^2H_{11/2} \rightarrow {}^4I_{15/2}$ emission intensity exhibits a monotonic increase up to 573K,which is likely stemming from energy transfer between Er^{3+} and Yb^{3+} and amplified by the thermal population exchange between $^2H_{11/2}$ and $^4S_{3/2}$.

Fig. 5a and d display the UC emission spectra of LMNO:0.01Er^{3+} and LMN:0.01Er^{3+},0.025 Yb^{3+} phosphors under 980 nm excitation at varying temperatures, with corresponding thermal evolution profiles shown in Fig. 5c and f. The temperature-dependent emission intensities at 527 nm ($^2H_{11/2} \rightarrow {}^4I_{15/2}$), 547 nm ($^4S_{3/2} \rightarrow {}^4I_{15/2}$) and 671 nm ($^4F_{9/2} \rightarrow {}^4I_{15/2}$) are illustrated in Fig. 5b and e. It is noteworthy that, in contrast to the DC case, the emission intensity at 527 nm for the Er^{3+} singly doped sample under 980 nm excitation remains nearly constant with increasing temperature. In contrast, upon Yb^{3+} co-doping, the emission intensity at 527 nm exhibits a non-monotonic trend, which increases initially, reaches a maximum at 423 K, and then decreases. This phenomenon likely originates from Yb^{3+}-enhanced thermal population exchange between the $^2H_{11/2}$ and $^4S_{3/2}$ levels of Er^{3+}, which elevates the quantum yield of the $^2H_{11/2} \rightarrow {}^4I_{15/2}$ transition.

Generally, the number of excited electrons in thermally coupled energy levels (TCLs) is related to the ambient temperature and obeys the Boltzmann distribution. To further study the temperature-detection ability of the samples, the FIR ratios of samples can be determined as follows [38,39]:

$$FIR = \frac{I_{up}}{I_{low}} = A \exp\left(-\frac{\Delta E}{k_B T}\right) \quad (1)$$

Here, I_{up} and I_{low} represent the emission intensities of the high energy level and the low energy level respectively. A is a constant independent of temperature, k_B is the Boltzmann constant and T is the absolute temperature. According to the Boltzmann distribution law, the temperature dependence of FIR between the transition intensity ratios of 527 ($^2H_{11/2} \rightarrow {}^4I_{15/2}$) and 547 ($^4S_{3/2} \rightarrow {}^4I_{15/2}$) in LMNO:0.01$Er^{3+}$ under 378 nm excitation was fitted (see Fig. 6a). The fitting degree, R^2, of FIR is 0.99764. With the help of the above equation, the ΔE value between the $^2H_{11/2}$ and $^4S_{3/2}$ energy levels is found to be 672 cm^{-1}, which is very consistent with value of 694 cm^{-1} that calculated according to the energy difference between $H_{11/2}$ and $^4S_{3/2}$ the energy level diagram. Absolute sensitivity (S_a) and relative sensitivity (S_r) are extremely important parameters for optical thermometers and can be expressed as follows [40,41]:

$$S_a = \left|\frac{d(FIR)}{dT}\right| = A \exp\left(-\frac{\Delta E}{k_B T}\right) \times \frac{\Delta E}{k_B T^2} \quad (2)$$

$$S_r = \left|\frac{d(FIR)}{(FIR)dT}\right| = \frac{\Delta E}{k_B T^2} \quad (3)$$

The temperature dependence of S_a and S_r values for sample LMNO:0.01Er^{3+} were shown in Fig. 6b. The S_a value initially increased with temperature, reaching a maximum of 0.679 % K^{-1} at 473 K, while S_r gradually decreased, peaking at 1.089 % K^{-1} at 298 K. Fig. 6c and d present the fitted FIR sensitivity values for LMNO:0.01Er^{3+},0.015 Yb^{3+}. The maximum S_a and S_r values can achieve 0.754 % K^{-1} and

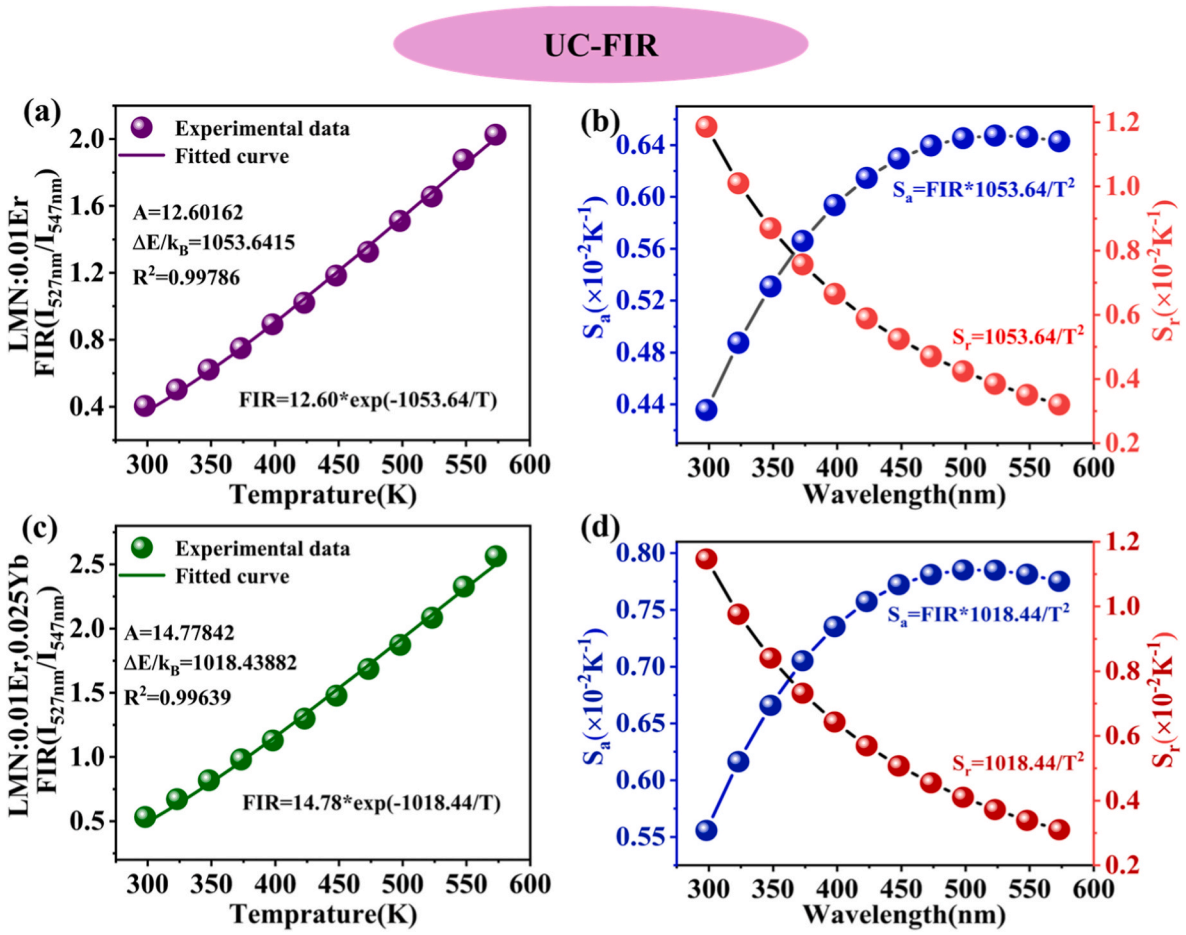

Fig. 7. FIR, S_a and S_r values calculated at different temperatures of (a, b) LMNO:0.01Er^{3+} and (c, d) LMNO:0.01Er^{3+},0.025 Yb^{3+} phosphor under 980 nm excitation.

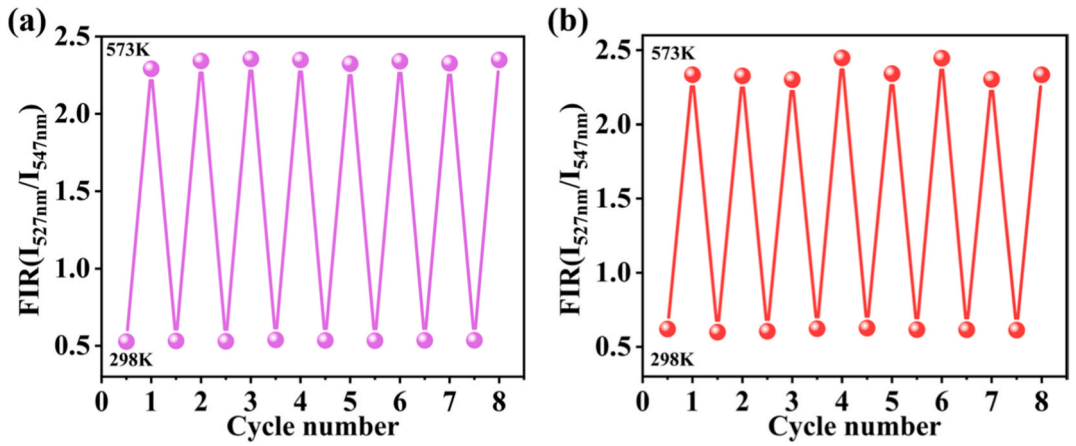

Fig. 8. (a) LMNO:0.01Er^{3+},0.015 Yb^{3+} under 378 nm excitation and (b) LMNO:0.01Er^{3+},0.025 Yb^{3+} under 980 nm excitation with eight thermal cycle measurements of FIR (I_{527nm}/I_{547nm}) for Er^{3+} ions.

1.162 % K^{-1}, respectively.

Moreover, LMNO:0.01Er^{3+} is also applicable for UC luminescence thermometry. Based on the FIR principle using Equations (1)–(3), the S_a and S_r values for LMNO:0.01Er^{3+} and LMNO:0.01Er^{3+},0.025 Yb^{3+} under 980 nm excitation were calculated (Fig. 7a–d). The maximum S_a and S_r for LMNO:0.01Er^{3+} reached 0.647 % K^{-1} and 1.19 % K^{-1}, respectively, while LMNO:0.01Er^{3+},0.025 Yb^{3+} exhibited enhanced S_a (0.785 % K^{-1}) and S_r (1.15 % K^{-1}). Analysis results reveal that in both DC and UC thermometry Yb^{3+} co-doping significantly enhances the luminescence intensity of Er^{3+} without compromising its thermometric sensitivity, which is highly advantageous for LMNO:Er^{3+},Yb^{3+} phosphors in optical thermometry applications.

In addition, repeatability (R) is a key parameter for optical temperature sensing application. Its expression can be defined as equation (4) [42]:

$$R = 1 - \frac{Max(\Delta_m - \Delta_i)}{\Delta_m} \tag{4}$$

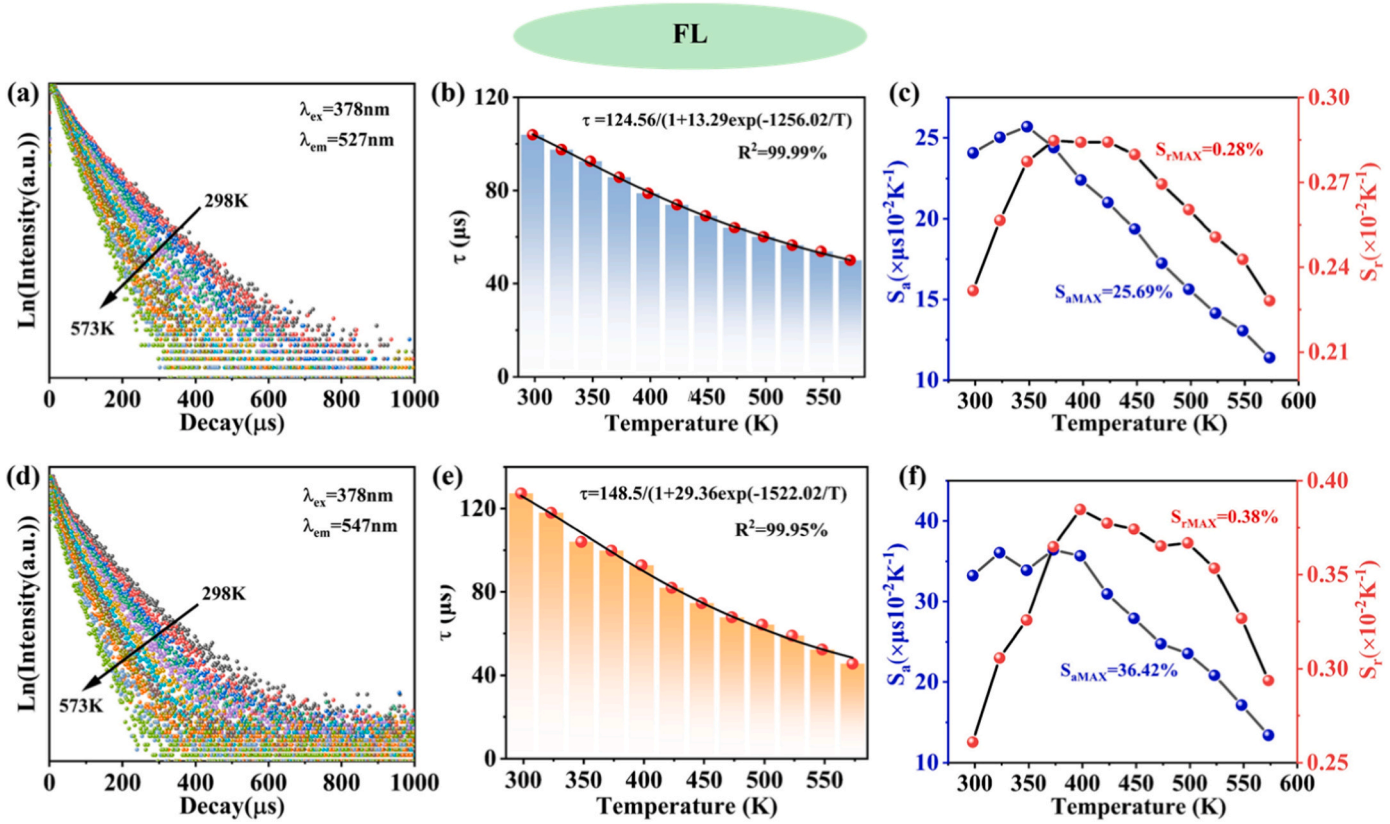

Fig. 9. The fluorescence decay lifetime curves of (a) 527 nm emission and (d) 547 nm emission and the average fluorescence decay lifetime of (b) 527 nm emission and (e) 547 nm emission of transition Er^{3+}: $^2H_{11/2} \rightarrow {}^4I_{15/2}$ under 378 nm excitation in the temperature range of 298 K–573K. The absolute sensitivity and relative sensitivity of (c) 527 nm and (f) 547 nm based on the fluorescence decay lifetime in the temperature region of 298 K–573 K.

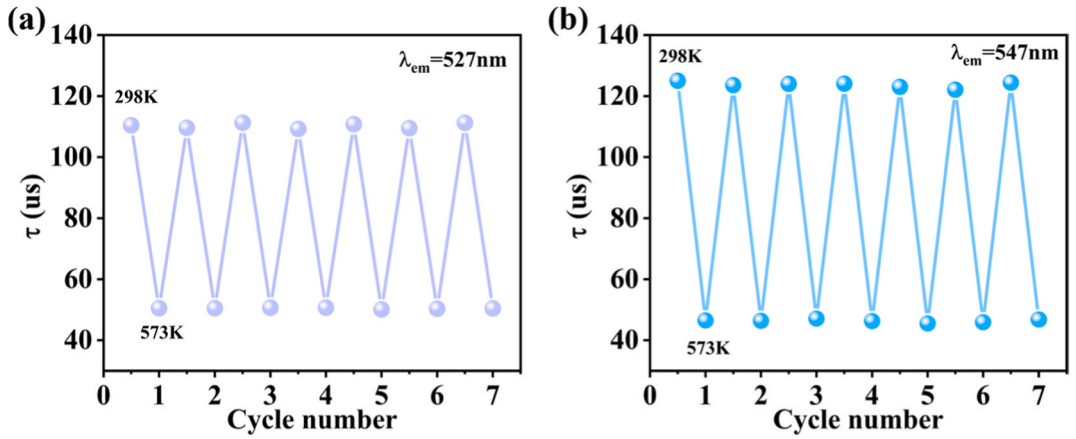

Fig. 10. Seven thermal cycle measurements of the fluorescence lifetime for LMNO:0.01Er^{3+} under 378 nm excitation at (a) 527 nm emission and (b) 547 nm emission.

Here, Δ_m and Δ_i represent the average value of FIR (at 303 K and 573 K) and the FIR value in eight consecutive irradiation cycles, respectively. Fig. 8 shows the cyclic measurement of FIR values of Er^{3+} in LMNO: 0.01Er^{3+}, 0.015 Yb^{3+} under 378 nm excitation and LMNO: 0.01Er^{3+}, 0.025 Yb^{3+} under 980 nm excitation, respectively. Excellent thermal repeatability (R > 99 %, calculated according to equation (4)) can be observed.

3.4. Temperature sensing based on FL thermometer

Beyond fluorescence intensity, FL provides an additional dimension for the internal calibration of results, thereby improving the precision of the measurement. Fig. 9a and d present the characteristic fluorescence decay curves of the Er^{3+} ions in the LMNO:0.01Er^{3+} sample. All lifetime decay curves were recorded under excitation at 378 nm and monitored at emission wavelengths of 527 nm and 547 nm, which were fitted using a biexponential function according to Equations (5) and (6):

$$I_t = I_0 + A_1 \exp\left(\frac{-t}{\tau_1}\right) + A_2 \exp\left(\frac{-t}{\tau_2}\right) \quad (5)$$

$$\tau = \left(A_1\tau^2 + A_2\tau^2\right) / \left(A_1\tau + A_2\tau\right) \quad (6)$$

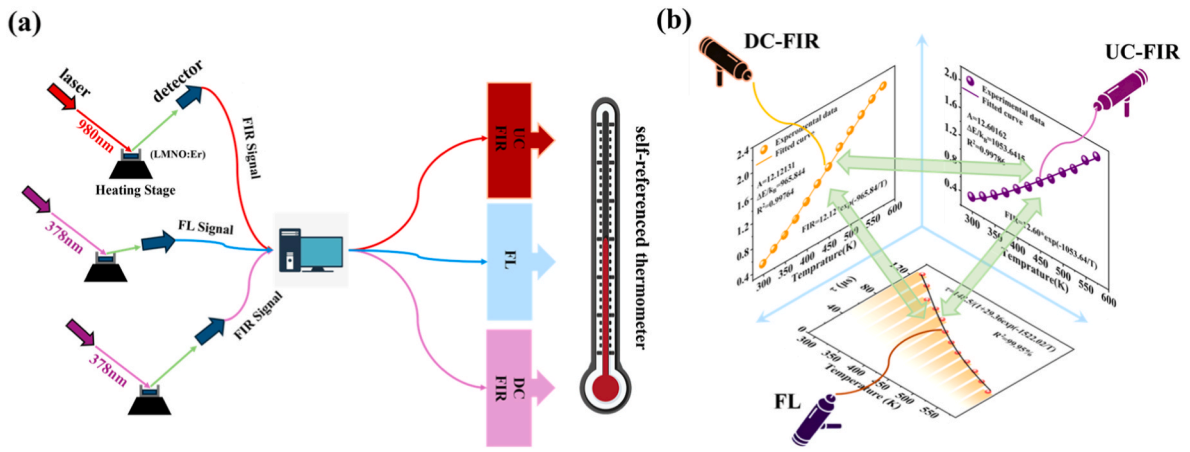

Fig. 11. Schematic diagram of a thermometer for self-referenced luminescence performance.

Here, A_1 and A_2 are constants, I_t and I_0 correspond to the fluorescence emission intensities at time t and the initial moment, respectively, and τ denotes the FL. The fitted average lifetimes, displayed in Fig. 9b and e, show a decrease for both the $^2H_{11/2}$ and $^4S_{3/2}$ energy levels with increasing temperature. This behavior can be attributed to the enhancement of nonradiative energy transfer processes. The temperature dependence of the lifetimes was fitted using the following Equation (7):

$$\frac{1}{\tau(T)} = \frac{1}{\tau_0}\left(1 + C\exp\left(\frac{-\Delta E}{k_B T}\right)\right) \tag{7}$$

Here, $\tau(T)$ represents the fluorescence lifetime at different temperatures and τ_0 denotes the lifetime value at 0 K [12]. ΔE is the energy gap between the $^4F_{7/2}$ and $^2H_{11/2}$ ($^4S_{3/2}$) levels. The fitting results are shown in Fig. 9c and f, with goodness of fit coefficients (R^2) of 99.91 % and 99.70 %, respectively. Furthermore, the Sr and Sa parameters based on the FL technique were calculated according to Equations (8) and (9):

$$S_a = \left|\frac{d\tau}{dT}\right| = \tau^2 \frac{C}{\tau_0}\frac{\Delta E}{k_B T^2}\exp\left(\frac{-\Delta E}{k_B T}\right) \tag{8}$$

$$S_r = \left|\frac{d\tau}{\tau dT}\right| = \tau \frac{C}{\tau_0}\frac{\Delta E}{k_B T^2}\exp\left(\frac{-\Delta E}{k_B T}\right) \tag{9}$$

For the temperature-dependent lifetimes of the $^2H_{11/2}$ and $^4S_{3/2}$ levels, the calculated Sa and Sr parameters both exhibit an initial increase followed by a decrease. As shown in Fig. 9c, the maxima Sa and Sr values for the $^2H_{11/2}$ level are 25.69 % μs K^{-1} and 0.28 % K^{-1}, respectively. For the $^4S_{3/2}$ level, the maxima Sa and Sr values are 36.42 % μs K^{-1} and 0.38 % K^{-1} as shown in Fig. 9f. Meanwhile, to evaluate the signal reproducibility and stability of fluorescence lifetime temperature sensing, the material was subjected to seven consecutive heating-cooling cycles, as shown in Fig. 10. The thermal repeatability R was calculated using Equation (4), and the results indicate excellent thermal repeatability (calculated R > 99 %).

The strong performance of DC-FIR, UC-FIR, and FL methods independently confirms that each is viable for temperature measurement on its own. More importantly, their built-in self-referencing ability comes from their distinct but connected physical pathways, which all start from the same excited states of the Er^{3+} ions. This multi-mode design allows the methods to cross-check each other when conditions are stable. Specifically, while DC-FIR and UC-FIR use different excitation sources, they both rely on the same thermal coupling between the $^2H_{11/2}$ and $^4S_{3/2}$ levels. If the temperatures they give disagree significantly, it could indicate a practical problem like localized heating or uneven sample concentration. In contrast, the FL lifetime provides a stable, non-ratio-based signal that is not affected by changes in excitation power or detection efficiency. This makes it a reliable reference for calibrating the intensity-based FIR signals. The real strength of this approach becomes clear when facing environmental interference. For example, if UV or NIR excitation becomes unstable and compromises either the DC or UC reading, the FL lifetime—which is robust against such power fluctuations—can work together with the other, unaffected FIR mode to still provide a trustworthy temperature value. In challenging or noisy conditions, a final, more reliable temperature reading can be calculated by combining the results from all three modes, taking into account the specific noise and known weaknesses of each, as depicted in Fig. 11. This combined strategy not only makes the measurement more trustworthy but also makes the whole system work reliably over a wider range of conditions than any single method could alone.

4. Conclusion

In summary, we synthesized LMNO:Er^{3+}/Yb^{3+} phosphors for self-referenced optical thermometry using three complementary signal modes: UC-FIR, DC-FIR, and FL. Under 378 nm and 980 nm excitation, the phosphors exhibited strong green emissions at 527 nm and 547 nm. Co-doping with Yb^{3+} significantly enhanced the UC and DC emission intensities of Er^{3+} by factors of 3 and 5, respectively. Higher emission intensity enhances the temperature sensing performance, thereby minimizing associated errors. The DC-FIR and UC-FIR modes achieved a maximum relative sensitivity of 1.16 % K^{-1} and 1.19 % K^{-1} respectively, while the FL mode yielded a high absolute sensitivity of 36.42 % μs K^{-1}. This integrated three-mode approach enables cross-validated temperature readout, effectively mitigating interference from light scattering and absorption, thus showcasing great potential for reliable luminescent thermometry.

CRediT authorship contribution statement

Wenliang Wu: Writing – original draft, Investigation, Data curation. **Lei Wang:** Supervision, Funding acquisition, Conceptualization. **Chenglan Huang:** Investigation. **Bingyan Qu:** Writing – original draft, Software, Data curation. **Caiping Zhu:** Formal analysis. **Junxiang Ding:** Validation, Formal analysis. **Hubertus T. Hintzen:** Validation, Formal analysis.

Declaration of competing interest

The authors declare that they have no known competing financial interests or personal relationships that could have appeared to influence the work reported in this paper.

Acknowledgments

This work is supported by the National Natural Science Foundation of China (Grant 52372143), Fundamental Research Funds for the Central Universities (PA2025GDGP0025, PA2024GDGP0042) and Structural Material Innovation for Expressway Median Barrier Panels (W2025JSKF0291).

Data availability

Data will be made available on request.

References

[1] M. Quintanilla, M. Henriksen-Lacey, C. Renero-Lecuna, L.M. Liz-Marzan, Challenges for optical nanothermometry in biological environments, Chem. Soc. Rev. 51 (11) (2022) 4223–4242.
[2] J. Zheng, B. Wu, F. Xu, T. Shan, X. Li, J. Tian, W. Zhang, An all-in-one PEGylated NIR-II conjugated polymer for high-resolution blood circulation imaging and photothermal immunotherapy, Biomaterials 317 (2025) 123107.
[3] Y. Ma, X. Zhou, J. Wu, Z. Dong, L. Cui, Y. Wang, A. Meijerink, Luminescence thermometry via multiparameter sensing in $YV_{1-x}P_xO_4$:Eu^{3+}, Er^{3+}, J. Am. Chem. Soc. 147 (15) (2025) 12925–12936.
[4] P. Kumar, R. Patel, N. Shrivastava, M. Patel, S. Rondeau-Gagné, G.S. Selopal, Aspects of luminescence nanoprobes for thermometry: progress and outlook, Appl. Mater. Today 35 (2023).
[5] H. Peng, M.I. Stich, J. Yu, L.N. Sun, L.H. Fischer, O.S. Wolfbeis, Luminescent Europium(III) nanoparticles for sensing and imaging of temperature in the physiological range, Adv Mater 22 (6) (2010) 716–719.
[6] Y. Hua, T. Wang, W. Xia, J.S. Yu, L. Li, Constructing novel red-emitting $Ba_2Y_{0.8}Eu_{0.2}NbO_6$:Mn^{4+} phosphors for multi-type luminescent thermometers and high-security anti-counterfeiting films, Mater. Today Chem. 23 (2022).
[7] L. Li, Y. Cao, H. Cui, G. Li, Y. Li, Y. Zhang, J. Zhang, B. Chen, Upconversion luminescence thermal enhancement from visible to near infrared and improving temperature sensitivity under high temperature using a second-harmonic generation response, Mater. Today Chem. 29 (2023).
[8] P. Du, J. Tang, W. Li, L. Luo, Exploiting the diverse photoluminescence behaviors of $NaLuF_4$:xEu^{3+} nanoparticles and g-C3N4 to realize versatile applications in white light-emitting diode and optical thermometer, Chem. Eng. J. 406 (2021).
[9] L. Ma, F. Lu, Q. Yu, P. Dai, F. Hu, H. Guo, R. Wei, A three-mode optical thermometry based on thermochromic Gd_2GaSbO_7:Bi^{3+},Eu^{3+} phosphors, Ceram. Int. 49 (11) (2023) 16681–16689.
[10] F. Lu, L. Wang, F. Hu, X. Tian, H. Guo, R. Wei, Multipath luminescent thermometry in $Cs_3GdGe_3O_9$:Yb^{3+}, Er^{3+} phosphor, Ceram. Int. 48 (24) (2022) 37186–37193.
[11] J. Xue, Z. Yu, H.M. Noh, B.R. Lee, B.C. Choi, S.H. Park, J.H. Jeong, P. Du, M. Song, Designing multi-mode optical thermometers via the thermochromic $LaNbO_4$:Bi^{3+}/Ln^{3+} (Ln = Eu, Tb, Dy, Sm) phosphors, Chem. Eng. J. 415 (2021).
[12] M. Dong, T. Yin, G. Guo, Z. Liu, F. Wang, C. Wang, L. Guan, X. Li, Three-mode optical thermometry based on multiresponsive $Ba_{1-x}Sr_xLaLiWO_6$:Er^{3+}, Yb^{3+} phosphors, Ceram. Int. 50 (1) (2024) 1050–1058.
[13] P. Du, J.S. Yu, Near-ultraviolet light induced visible emissions in Er^{3+} -activated La_2MoO_6 nanoparticles for solid-state lighting and non-contact thermometry, Chem. Eng. J. 327 (2017) 109–119.
[14] Y. Jiang, Y. Tong, S. Chen, W. Zhang, F. Hu, R. Wei, H. Guo, A three-mode self-referenced optical thermometry based on up-conversion luminescence of Ca_2MgWO_6:Er^{3+},Yb^{3+} phosphors, Chem. Eng. J. 413 (2021).
[15] J. Wang, H. Lin, Y. Cheng, X. Cui, Y. Gao, Z. Ji, J. Xu, Y. Wang, A novel high-sensitive upconversion thermometry strategy: utilizing synergistic effect of dual-wavelength lasers excitation to manipulate electron thermal distribution, Sensor. Actuator. B Chem. 278 (2019) 165–171.
[16] M. Fu, Z. Fan, P. Qiao, L. Hu, D. Deng, S. Xu, H. Ma, Optical properties of La_2LiSbO_6:Bi^{3+}/Er^{3+} phosphor for multicolor anti-counterfeiting and dual-mode optical thermometry, Ceram. Int. 51 (20) (2025) 30078–30085.
[17] X. Wang, X. Li, H. Yu, S. Xu, J. Sun, L. Cheng, X. Zhang, J. Zhang, Y. Cao, B. Chen, Effects of Bi^{3+} on down-/up-conversion luminescence, temperature sensing and optical transition properties of Bi^{3+}/Er^{3+} co-doped $YNbO_4$ phosphors, J. Rare Earths 40 (3) (2022) 381–389.
[18] A.M. Voiculescu, S. Hau, G. Stanciu, C. Gheorghe, A dual-mode temperature sensing based on UC luminescence of a new green Er^{3+}: $SrLaGaO_4$ phosphor, J. Alloys Compd. 1038 (2025).
[19] F. Ayachi, K. Saidi, M. Dammak, W. Chaabani, I. Mediavilla-Martínez, J. Jiménez, Dual-mode luminescence of Er^{3+}/Yb^{3+} codoped $LnP_{0.5}V_{0.5}O_4$ (Ln=Y, Gd, La) for highly sensitive optical nanothermometry, Mater. Today Chem. 27 (2023).
[20] Z. Lv, X. Shi, C. Wang, B. Zhang, D. Zhang, F. Wang, X. Wang, Z. Zhou, X. Yang, L. Ying, J. Zhu, Y. Huang, D. Zhang, Achieving multiwavelength optical amplification based on polymer waveguides doped with $NaYF_4$:Er^{3+}, Yb^{3+} nanoparticles under commercial and convenient led pumping, Adv. Mater. Technol. 9 (7) (2024).
[21] T.B. Ivetić, B. Banjac, L. Đačanin Far, D. Štrbac, Z. Ristić, Er^{3+}/Yb^{3+} co-activated $YNbO_4$ nanocrystalline phosphors: Up-conversion luminescence under the 980 nm excitation and integrated lifetime thermometry, Opt. Mater. 169 (2026).
[22] S. Kapuri, L. Mukhopadhyay, V.K. Rai, Negative thermal quenching effect in Er^{3+}/Yb^{3+}: Ca_2ZnWO_6 phosphors: towards optical thermometry and anti-counterfeiting applications, Mater. Res. Bull. 193 (2026).
[23] G. Zhang, S. Xu, X. Li, R. Wang, H. Zhang, C. Su, Up-conversion luminescence properties and temperature sensing of Er^{3+}/Yb^{3+} doped silicate glass-ceramics, Ceram. Int. 51 (2) (2025) 2173–2183.
[24] S.F. León-Luis, U.R. Rodríguez-Mendoza, P. Haro-González, I.R. Martín, V. Lavín, Role of the host matrix on the thermal sensitivity of Er^{3+} luminescence in optical temperature sensors, Sensor. Actuator. B Chem. 174 (2012) 176–186.
[25] S. Liu, L. Zhong, Y. Xiang, Z. Chen, M. Xie, J. Hong, L. Zhou, M. Wu, Developing high-performance Ca2LaNbO6 phosphors Co-doped with Bi3+ and Eu3+ for multi-color emission and temperature sensing, Mater. Today Chem. 44 (2025).
[26] Z. Tian, X. Peng, R. Li, W. Chen, K. Wang, X. Guo, R. Cui, Er^{3+} activation double perovskite green trifunctional material for dual-mode optical thermometry, lighting technology and fingerprint detection, Mater. Today Chem. 48 (2025).
[27] Y. Tian, Y. Tian, P. Huang, L. Wang, Q. Shi, C.e. Cui, Effect of Yb^{3+} concentration on upconversion luminescence and temperature sensing behavior in Yb^{3+}/Er^{3+} co-doped $YNbO_4$ nanoparticles prepared via molten salt route, Chem. Eng. J. 297 (2016) 26–34.
[28] J.-S. Kim, C.-I. Cheon, H.-J. Kang, H.-S. Shim, C.-H. Lee, S. Nam, J.-D. Byun, Crystal structure of $La(Mg_{2/3}M_{1/3})O_3$ (M=Nb,Ta) microwave dielectric ceramics, Mater. Lett. 38 (4) (1999) 294–299.
[29] H. Dong, Z. Lei, S. Su, W. Yang, X. Zhang, W. Teng, G. Zu, B. Teng, D. Zhong, Achieving high-sensitivity dual-mode optical thermometry via phonon-assisted cross-relaxation in a double-perovskite structured up-conversion phosphor, Inorg. Chem. Front. 11 (9) (2024) 2784–2797.
[30] Z. Lei, H. Dong, L. Sun, B. Teng, Y. Zou, D. Zhong, Eulytite-type $Ba_3Yb(PO_4)_3$:Tm/Er/Ho as a high sensitivity optical thermometer over a broad temperature range, J. Mater. Chem. C 12 (2) (2024) 628–638.
[31] Z. Yang, M. Ye, S. Yang, R. Wang, C. Sun, Y. Li, J. Wang, Efficient and abnormal thermal quenching Sm^{3+} activated perovskites-type niobate phosphor for plant growth lamp and WLEDs, Ceram. Int. 50 (12) (2024) 21745–21754.
[32] Z. Yang, M. Ye, C. Sun, J. Zhao, H. Bu, S. Yang, R. Wang, Highly sensitive dual-mode temperature measurement utilizing completely opposite thermal quenching luminescence, Ceram. Int. 50 (22) (2024) 44833–44842.
[33] R.D. Shannon, Revised effective ionic radii and systematic studies of interatomic distances in halides and chalcogenides, Acta Crystallogr. Sect. A Found. Crystallogr. 32 (5) (1976) 751–767.
[34] X. Jiang, Y. Guo, L. Wang, Q. Zhang, Novel multi-mode anti-counterfeiting encryption material of $CaAl_{12}O_{19}$:Eu, Er with multi-color down-conversion luminescence, up-conversion luminescence, dynamic luminescence and photochromism, J. Colloid Interface Sci. 678 (Pt A) (2025) 872–885.
[35] M. Bouzidi, A. Maaoui, N. Chaaben, A.S. Alshammari, Z.R. Khan, M. Mohamed, Downconversion mechanism in Er^{3+}/Yb^{3+} codoped fluorotellurite glasses to enhance the efficiency of c-Si PV cells, J. Non-Cryst. Solids 595 (2022).
[36] M. Li, L. Su, X. Chen, Q. Wu, B. Zhang, Effect of Yb^{3+} concentration on Er^{3+} doped CaF_2 single crystal for temperature sensor applications, Opt. Commun. 520 (2022).
[37] Y. Chen, J. Chen, Y. Tong, W. Zhang, X. Peng, H. Guo, D. Huang, Y_4GeO_8:Er^{3+},Yb^{3+} up-conversion phosphors for optical temperature sensor based on FIR technique, J. Rare Earths 39 (12) (2021) 1512–1519.
[38] Y. Hua, J.S. Yu, Thermal-couple levels of $^4S_{3/2}$ and $^2H_{11/2}$ in Na(Ca, Sr)$La(VO_4)_2$: Er^{3+} phosphors for potential optical thermometers, J. Am. Ceram. Soc. 103 (12) (2020) 7082–7094.
[39] G. Xiang, Y. Yi, Z. Yang, Y. Wang, L. Yao, S. Jiang, X. Zhou, L. Li, X. Wang, J. Zhang, Achieving ultrasensitive temperature sensing through non-thermally coupled energy levels to overcome energy gap constraints, Inorg. Chem. Front. 11 (5) (2024) 1522–1530.
[40] Y. Peng, D. Chen, J. Zhong, X. Li, Q. Mao, F. Chi, Lanthanide-doped KGd_3F_{10} nanocrystals embedded glass ceramics: Self-crystallization, optical properties and temperature sensing, J. Alloys Compd. 767 (2018) 682–689.
[41] J. Zhang, Y. Zhang, X. Jiang, Investigations on upconversion luminescence of $K_3Y(PO_4)_2$:Yb^{3+}-Er^{3+}/Ho^{3+}/Tm^{3+} phosphors for optical temperature sensing, J. Alloys Compd. 748 (2018) 438–445.
[42] D. Guo, Z. Wang, N. Wang, B. Zhao, Z. Li, J. Chang, P. Zhao, Y. Wang, X. Ma, P. Li, H. Suo, Doping-mediated thermal control of phase transition for supersensitive ratiometric luminescence thermometry, Chem. Eng. J. 492 (2024).
[43] M.D. Dramićanin, Sensing temperature via downshifting emissions of lanthanide-doped metal oxides and salts. A review, Methods Appl. Fluoresc. 4 (4) (2016) 042001.
[44] L. Tong, X. Li, R. Hua, L. Cheng, J. Sun, J. Zhang, S. Xu, H. Zheng, Y. Zhang, B. Chen, Optical temperature sensing properties of Yb^{3+}/Tm^{3+} co-doped $NaLuF_4$ crystals, Curr. Appl. Phys. 17 (7) (2017) 999–1004.
[45] P. Du, L. Luo, W. Li, Q. Yue, Upconversion emission in Er-doped and Er/Yb-codoped ferroelectric $Na_{0.5}Bi_{0.5}TiO_3$ and its temperature sensing application, J. Appl. Phys. 116 (1) (2014).
[46] D. Chen, L. Zhang, Y. Liang, W. Wang, S. Yan, J. Bi, K. Sun, Yolk–shell structured Bi_2SiO_5:Yb^{3+},Ln^{3+} (Ln = Er, Ho, Tm) upconversion nanophosphors for optical thermometry and solid-state lighting, CrystEngComm 22 (26) (2020) 4438–4448.
[47] A. Torquato, R.A. de Oliveira, T.O. Sales, G.Y. Poirier, G. Batista, F.C. Cassanjes, C. Jacinto, M.R. Dousti, Influence of PbF_2 content on optical thermometry of Er^{3+}/Yb^{3+} co-doped tungsten sodium phosphate glasses, Opt. Mater. 112 (2021).
[48] X. Zhu, X. Huang, C. He, F. Lin, X. Liu, Y. Yang, C. Yang, Z. Huang, X. Min, R. Mi, Synthesis and characterization of Er^{3+}-Doped $SrNb_2O_6$ phosphor for FIR based thermometer, ECS J. Solid State Sci. Technol. 10 (4) (2021).

[49] J. Liu, W. Huang, Z. Xia, Y. Xu, Facile synthesis of accordion-like $Y_2O_3:Er^{3+}$ nanothermometers for ratiometric temperature sensing applications, J. Lumin. 223 (2020).

[50] J. Hu, X. Zhang, H. Zheng, F. Lu, X. Peng, R. Wei, F. Hu, H. Guo, Improved photoluminescence and multi-mode optical thermometry of Er^{3+}/Yb^{3+} co-doped $(Ba,Sr)_3Lu_4O_9$ phosphors, Ceram. Int. 48 (3) (2022) 3051–3058.

[51] X. Yang, Y. Zhu, T. Li, S. Long, B. Wang, High-accuracy dual-mode optical thermometry based on up-conversion luminescence in Er^{3+}/Ho^{3+}-Yb^{3+} doped $LaNbO_4$ phosphors, Ceram. Int. 49 (13) (2023) 21932–21940.